Room Temperature Carbon Monoxide Oxidation over Two-Dimensional Gold-Loaded Mesoporous Iron Oxide Nanoflakes

SCHOLARONE™
Manuscripts

Chemical Communication

Room Temperature Carbon Monoxide Oxidation over Two-Dimensional Gold-Loaded Mesoporous Iron Oxide Nanoflakes

Yusuf Valentino Kaneti,[a†] Shunsuke Tanaka,[a,b†] Yohei Jikihara,[c] Tsuruo Nakayama,[c] Yoshio Bando,[a,b] Masatake Haruta,[d] Md. Shahriar A. Hossain,[e] Dmitri Golberg,[f] and Yusuke Yamauchi[e,g]*

In this work, we fabricate a highly effective catalyst for carbon monoxide oxidation based on gold-loaded mesoporous maghemite nanoflakes which exhibit nearly 100% CO conversion and a very high specific activity of 8.41 mol_{CO} g_{Au}^{-1} h^{-1} at room temperature. Such excellent catalytic activity is promoted by the synergistic cooperation of their high surface area, large pore volume, and mesoporous structure.

Human activities, such as chemical combustion, vehicle exhausts, and the burning of fossil fuels for electricity generation have contributed significantly to the release of carbon monoxide (CO) into the atmosphere. The presence of a high concentration of CO in the atmosphere can lead to respiratory illnesses, nausea, dizziness, and even death due to its highly toxic nature.[1] As such, it is highly desirable to convert CO into carbon dioxide (CO_2), which is a less toxic gas commonly used in methanol production. Noble metal catalysts, *e.g.*, Pt, Pd, Au, *etc.*, have been shown to exhibit high catalytic activity for CO oxidation.[2-4] However, due to their high cost and scarcity, it is highly desirable to load them onto metal oxide supports to reduce the amount of the noble metal catalyst. Furthermore, these noble metals only exhibit high catalytic activity for CO oxidation above ~150 °C.[2] Since the pioneering study by Haruta *et al*.[5] which revealed the high catalytic activity of oxide-supported gold nanoparticles (Au NPs) at lower temperatures, many studies have been aimed at developing heterogeneous catalysts for room temperature CO oxidation. However, it is still challenging to achieve a high CO conversion (>70%)

with oxide supported Au NPs at room temperature without any pre-treatment or humidity control.[6]

Among various oxides, iron oxides (Fe_xO_y) are one of the most popular support materials due to their low cost, wide abundance, and high thermal and chemical stabilities.[7] In oxide-supported Au NPs, the size, shape and porosity of the support materials can significantly influence the dispersion of the Au NPs and therefore, the overall catalytic activity.[8] Mesoporous two-dimensional (2D) oxides have gained increasing interest in heterogeneous catalysis owing to their high surface area, large pore volume, improved catalytic activity, and enhanced thermal stability.[9] In addition, mesoporous oxides have the capability to interact with gas molecules both at their exterior surface and within the large interior surface of the material.[8] To date, porous iron oxide materials with crystalline walls have been synthesized through template-based approaches using mesoporous silica,[10] metal-organic frameworks,[11] surfactants,[12] and block copolymers.[9, 13] However, it is still relatively difficult to synthesize small-sized 2D mesoporous iron oxide materials (≤100 nm) with high surface area (~200 m^2 g^{-1}) without the use of templates or toxic/organic precursors.

In this communication, we report the facile fabrication of mesoporous maghemite (γ-Fe_2O_3) nanoflakes as support materials for Au NPs *via* solvothermal method. Owing to their high surface area (up to 193 m^2 g^{-1}) and large pore volume, these nanoflakes can store up to 15 wt% Au and their meseporous structure enables well dispersion of Au NPs throughout the support. When employed as a catalyst for CO oxidation, the optimized Au-loaded mesoporous γ-Fe_2O_3 nanoflakes show >95% CO conversion and high specific activity of 8.41 mol_{CO} g_{Au}^{-1} h^{-1} at room temperature. Their high catalytic activity toward CO oxidation is attributed to the synergistic cooperation of their high surface area, large pore volume, and mesoporous nature.

Fig. S1 shows the scanning electron microscopy (SEM) images of the product obtained from the solvothermal treatment of iron(III) nitrate and glycerol in 2-propanol at 180 ºC. Evidently, the product exhibits uniform flake-like morphology with small diameters of around 60-100 nm. Our parametric investigation reveals that the obtained nanoflakes become more separated and well-defined with increasing amount of glycerol, with the optimal amount being 10 mL (**Fig. S2**). The FTIR spectrum of the precursor nanoflakes reveals the presence of several strong peaks (**Fig. 1a**). The broad peak observed at 3350 cm^{-1} and the peaks in the range of 2650-2950 cm^{-1} can be

[a.] *International Center for Materials Nanoarchitectonics (MANA), National Institute for Materials Science (NIMS), 1-1 Namiki, Tsukuba, Ibaraki 305-0044, Japan.*
[b.] *Australian Institute of Innovative Materials (AIIM), University of Wollongong, North Wollongong, New South Wales 2500, Australia.*
[c.] *NBC Meshtec Inc., 2-50-3 Toyoda, Hino-shi, Tokyo, 191-0053, Japan.*
[d.] *Research Center for Gold Chemistry, Tokyo Metropolitan University, 1-1-F203 Minami-Osawa, Hachioji, Tokyo, 192-0397, Japan.*
[e.] *School of Chemical Engineering and Australian Institute for Bioengineering and Nanotechnology (AIBN), The University of Queensland, Brisbane, QLD 4072, Australia. Email: y.yamauchi@uq.edu.au*
[f.] *School of Chemistry, Physics and Mechanical Engineering, Science and Engineering Faculty, Queensland University of Technology (QUT), Brisbane, Queensland 4000, Australia*
[g.] *Department of Plant & Environmental New Resources, Kyung Hee University, 1732 Deogyeong-daero, Giheung-gu, Yongin-si, Gyeonggi-do 446-701, South Korea.*
† These authors contributed equally to this work

attributed to the O-H stretching and C-H stretching vibrations, respectively.[14] The H-O-H scissor mode observed at 1674 cm^{-1} represents water on their surface.[15] The peaks located between 1355-1465 cm^{-1} and 900-1300 cm^{-1} are assignable to C-H bending and C-O stretching vibrations, respectively.[16] Moroever, the peaks detected between 700-900 cm^{-1} are characteristics of iron multivalent-state interactions. The presence of distinct peaks in the range of 1000–1125 cm^{-1} and 2800-2900 cm^{-1} indicate that precursor product can be assigned as iron glycerate nanoflakes.[17] Thermogravimetric (TG) curve of the iron glycerate nanoflakes from room temperature to 800 ºC reveals three weight loss steps (**Fig. S3**). The first weight loss step in the temperature range of 25-200 ºC is attributed to the evaporation of both physisorbed and chemisorbed water.[14] The second weight loss step between 200-250 ºC corresponds to the removal of organic constituents in the nanoflakes.
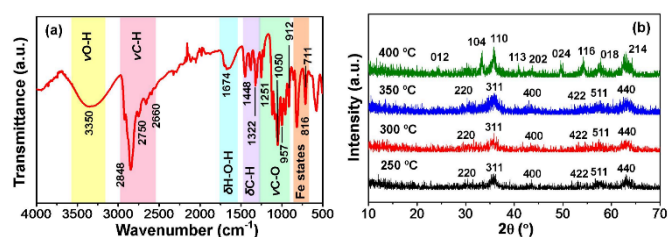

Fig. 1. (a) Fourier transform infrared (FTIR) spectrum of the precursor nanoflakes. (b) X-ray-diffraction (XRD) patterns of the iron oxide nanoflakes obtained at various calcination temperatures.

To convert to iron oxides, these precursor nanoflakes were calcined at different temperatures from 250 to 400 °C and the samples are labeled as Fe-MNF-250, Fe-MNF-300, Fe-MNF-350, and Fe-MNF-400, respectively. The XRD patterns of these samples are given in **Fig. 1b**. Surprisingly, the formation of γ-Fe$_2$O$_3$ phase is already observed at a calcination temperature as low as 250 °C, as indicated by the presence of (220), (311), (400), (422), (511), and (440) planes of γ-Fe$_2$O$_3$ (JCPDS No. 39-1346). Evidently, the γ-Fe$_2$O$_3$ peaks become more intense with increasing calcination temperature up to 350 °C, suggesting the increase in crystallinity. However, the product obtained at 400 °C can instead be indexed to hematite (α-Fe$_2$O$_3$) phase, as confirmed by the presence of (012), (104), (110), (113), (024), (116), (122), (214), and (300) planes of $α$-Fe$_2$O$_3$ (JCPDS No. 33-664).

The corresponding SEM images of the calcined products are given in **Fig. 2**. The original flake-like shape of the iron glycerate nanoflakes is well-preserved up to 350 °C (**Fig. 2a-c**), however, serious sintering of the nanoflakes is observed at 400 °C (**Fig. 2d**), which may be correlated to the phase transformation from γ-Fe$_2$O$_3$ to α-Fe$_2$O$_3$. The high-resolution TEM (HRTEM) image of the γ-Fe$_2$O$_3$ nanoflakes (Fe-MNF-350) displays lattice fringes with a *d*-spacing of 0.25 nm, indexed to the *d*-spacing of γ-Fe$_2$O$_3$(311) (**Fig. S4**). The selected area electron diffraction (SAED) pattern of these nanoflakes indicates their polycrystalline nature, as shown in the inset of **Fig. S4b**.

The iron oxide nanoflakes obtained at different calcination temperatures were then loaded with Au NPs *via* deposition-precipitation method and the SEM images of the resulting composites are given in **Fig. S5**. The presence of well-dispersed Au NPs with sizes of 2-5 nm can be seen from the transmission electron microscopy (TEM) images of a typical sample, such as Au/Fe-MNF-350, as shown in **Fig. 3a**. This size range falls well within the optimum size of supported Au NPs for CO oxidation.[18] The HRTEM image of the Au-loaded mesoporous γ-Fe$_2$O$_3$ nanoflakes (Au/Fe-MNF-350) shows

clear lattice fringes with *d*-spacings of 0.25 nm and 0.23 nm, indexed to γ-Fe$_2$O$_3$(311) and Au(111) planes, respectively (**Fig. 3b**). The good dispersion of the deposited Au NPs on the γ-Fe$_2$O$_3$ support is confirmed by the HAADF-TEM image and energy dispersive spectroscopy (EDS) mapping shown in **Fig. 3c-f**.

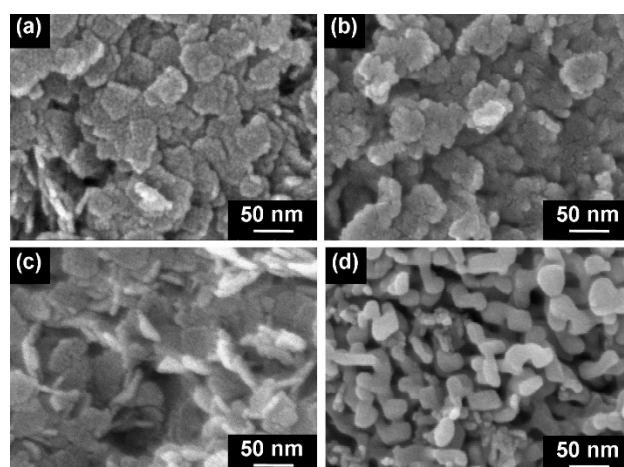**Fig. 2.** SEM images of the mesoporous iron oxide nanoflakes obtained at calcination temperatures of (a, b) 250 °C, (c, d) 300 °C, (e, f) 350 °C, and (g, h) 400 °C.
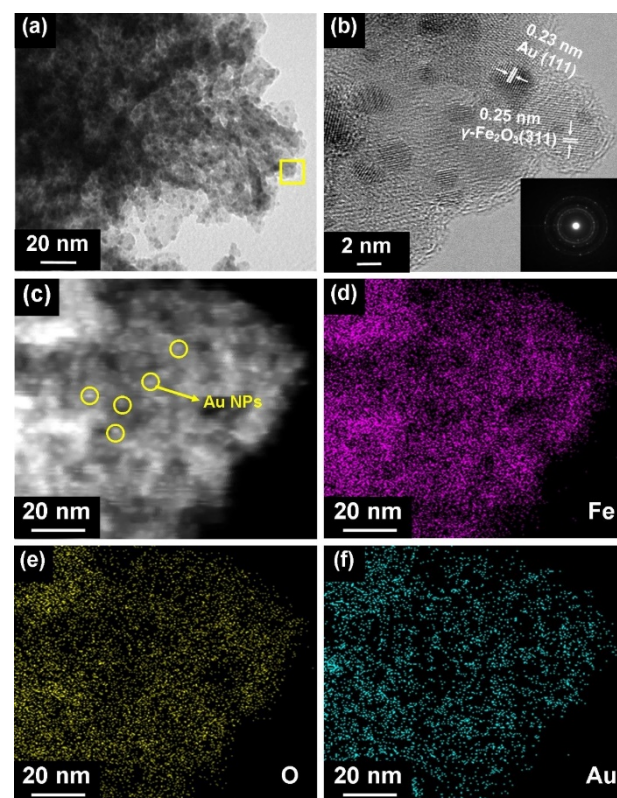

Fig. 3. (a) TEM and (b) HRTEM images of Au/Fe-MNF-350 (inset shows the corresponding SAED patterns). (c) High angle annular dark field (HAADF) TEM image of Au/Fe-MNF-350 and the corresponding EDS mapping for (d) Fe, (e) O, and (f) Au.

The XRD patterns of all the Au-loaded iron oxide samples clearly show the presence of Au(111), Au(200), and Au(220) planes (JCPDS No. 04-784) (**Fig. 4a**). **Fig. 4b** presents the X-ray photoelectron spectroscopy (XPS) survey spectra of the γ-Fe$_2$O$_3$ nanoflakes

obtained at 350 °C before (Fe-MNF-350) and after loading with Au NPs (Au/Fe-MNF-350). Prior to the Au loading, only Fe2p and O1s peaks are observed in the survey spectrum of Fe-MNF-350. After the Au loading, the Au4f peak is clearly observed in the survey spectrum of Au/Fe-MNF-350, confirming the successful deposition of Au NPs onto the γ-Fe$_2$O$_3$ nanoflakes. Further XPS analysis is given in **Fig. S6**.
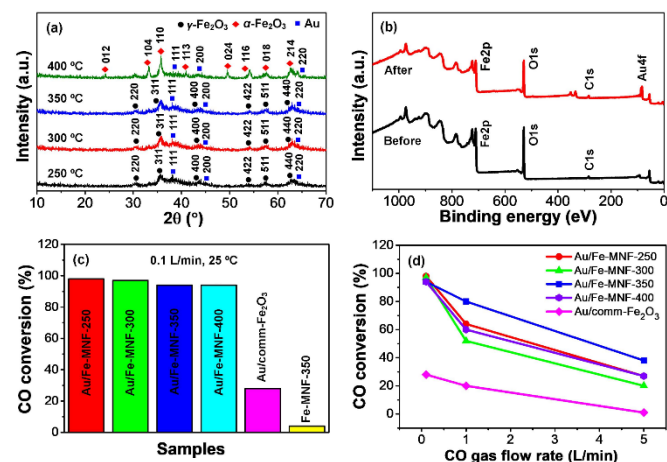

Fig. 4. *(a) XRD patterns of the Au-loaded mesoporous iron oxide nanoflakes obtained at different calcination temperatures. (b) XPS survey spectra of Fe-MNF-350 and Au/Fe-MNF-350. (c) CO conversion efficiencies of pure Fe-MNF, Au/Fe-MNF, and Au/commercial Fe$_2$O$_3$ sample at 25 °C under CO gas flow of 0.1 L min^{-1} and humidity level of 60%. (d) The influence of CO gas flow rate on the CO conversion of these samples at 25 ºC. The amount of catalyst is 4 mg, except for the Au-loaded commercial Fe$_2$O$_3$ (40 mg) due to its low conversion efficiency.*

The N$_2$ adsorption-desorption isotherms of all the calcined samples display a type IV hysteresis loop, indicating their mesoporous nature (**Fig. S7**). The specific surface areas of Fe-MNF-250, Fe-MNF-300, Fe-MNF-350, and Fe-MNF-400 are 193, 153, 140, and 130 m^2 g^{-1}, and the corresponding pore volumes of these samples are 0.57, 0.53, 0.48, and 0.52 cm^3 g^{-1}, respectively (**Table S1**). Evidently, the specific surface area decreases with increasing calcination temperature, which is caused by the increase in pore size of the particles, as seen in **Fig. S7**.

The Au-loaded mesoporous iron oxide nanoflakes were subsequently used as catalysts for CO oxidation. The amount of Au loading on the mesoporous iron oxide nanoflakes obtained at different calcination temperatures (250-400 °C) and commercial Fe$_2$O$_3$ sample was analyzed by inductively coupled plasma optical emission spectrometry (ICP-OES). The results reveal that all the synthesized mesoporous iron oxide nanoflakes could store a large amount of Au NPs of $\geq$ 10 wt% (**Table S2**). Evidently, the amount of Au loading decreases with increasing calcination temperature which is due to the decrease of the surface area. In contrast, the amount of Au loading on the commercial Fe$_2$O$_3$ sample is very small (0.81 wt% Au). The much higher loading of Au NPs on the mesoporous Fe$_2$O$_3$ nanoflakes relative to the commercial Fe$_2$O$_3$ may be contributed by their higher surface areas which enable the accommodation of a larger number of Au NPs while also decreasing their density, thus reducing their aggregation. Another possible reason is the higher amount of surface defects (*e.g.*, steps, edges and kinks) present on the mesoporous Fe$_2$O$_3$ nanoflakes relative to the commercial Fe$_2$O$_3$ particles, as Au NPs cannot easily adsorb on a flat metal oxide surface.[7]

The CO oxidation catalytic tests were conducted under similar gas hourly space velocity (GHSV). As shown in **Fig. 4c**, all the Au-loaded mesoporous iron oxide samples show high conversion efficiencies of over 90% even at room temperature under 0.1 L min^{-1} of CO gas flow. In comparison, the CO conversion achieved using the Au-loaded commercial Fe$_2$O$_3$ sample is much lower at around 28%, while the pristine Fe-MNF350 sample shows negligible catalytic activity with CO conversion of around 4%. The catatytic activity of all the Au-loaded mesoporous iron oxide samples decreases when CO gas flow rate was increased to 1 L min^{-1}, however they still show CO conversion of over 50%, with the sample Au/Fe-MNF-350 exhibiting the highest CO conversion of around 80% (**Fig. 4d**). With a further increase of the flow rate to 5 L min^{-1}, the samples Au/Fe-MNF-250, Au/Fe-MNF-300, and Au/Fe-MNF-400 exhibit CO conversion of less than 30%, however, the Au/Fe-MNF-350 sample still display a competitive CO conversion of around 40%. The decrease in CO conversion with increasing CO flow rate is due to the decreased residence time of the reactants on the surface of the catalyts.[19] The specific activities of the Au-loaded mesoporous iron oxide samples were calculated and compared with previously reported Au/Fe$_x$O$_y$ catalysts, as summarized in **Table S2**. The trend in CO conversion efficiency (mol$_{CO}$ g$_{Au}^{-1}$ h^{-1}) is in the order of Au/Fe-MNF-350 (8.41)> Au/Fe-MNF-400 (7.67)> Au/Fe-MNF-250 (4.93)> Au/Fe-MNF-300 (4.38). Interestingly, despite the higher Au loading and surface area of samples Au/Fe-MNF-250 and Au/Fe-MNF-300, the samples Au/Fe-MNF-350 and Au/Fe-MNF-400 exhibit higher specific activities. This may be attributed to their higher crystallinity as the catalytic performance of oxide-supported Au NPs is strongly affected by the degree of crystallinity of the oxide support.[20]

From **Table S2**, it is clear that the Au/Fe-MNF-350 catalyst show much higher specific activity for CO oxidation compared to Au-loaded commercial Fe$_2$O$_3$, as well as superior activities to many previously reported Au/Fe$_2$O$_3$, Au/CeO$_2$, and Au/γ-Al$_2$O$_3$ catalysts. Recyclability data of the Au/Fe-MNF-350 catalyst is given in **Fig. S8**. The excellent catalytic activity of these samples for CO oxidation at room temperature is attributed to the synergistic cooperation of various factors. First, the high surface area and large pore volume exhibited by the mesoporous γ-Fe$_2$O$_3$ nanoflakes offer many reaction sites for the reactants during the catalytic reaction. In Au-supported iron oxide catalysts, the reactive site is typically around the Au/γ-Fe$_2$O$_3$ interface.[21] As our iron oxide supports are highly porous, more defect sites (*e.g.*, steps, edges, corners, and kinks) are present on their structures compared to a non-porous support, which serve as additional active sites for the adsorption of reactants.[7] Hence, during the CO oxidation, oxygen is also adsorbed on these defect sites in addition to the deposited Au NPs and react with CO to produce CO$_2$. This in turn increases the reaction rate due to the improved oxygen activation rate. Furthermore, the 2D mesoporous structure of the γ-Fe$_2$O$_3$ supports along with the ideal pore sizes enables well dispersion of the Au NPs throughout the support and prevent their agglomeration despite the high loading amount, as seen in **Fig. 3**. This in turn enhances the contact between the support and the Au NPs, leading to stronger support-metal electronic interaction and higher catalytic activity.[22] In addition, the presence of mesopores can improve the diffusivity of the reactant molecules during the CO oxidation reaction, further enhancing the overall catalytic activity. Another potential reason for the improved catalytic activity is the presence of cationic gold in our catalysts, which has been thought to be active for CO oxidation.[23] Lastly, the size range of the deposited Au NPs is 2-5 nm which falls well within the ideal size of Au NPs for achieving the maximum catalytic activity for CO oxidation (3.5 nm),

as suggested by Goodman *et al*.[18] Such an ideal size range is beneficial for increasing the perimeter length of the $Au/\gamma\text{-}Fe_2O_3$ interface, (*i.e.*, active sites) and therefore the overall catalytic activity.[24]

In conclusion, we have successfully synthesized a highly effective catalyst for CO oxidation based on Au-loaded mesoporous $\gamma\text{-}Fe_2O_3$ nanoflakes which exhibit over 90% CO conversion and high specific activity of 8.41 mol_{CO} g_{Au}^{-1} h^{-1} at room temperature, which is among the highest ever reported for Au/Fe_xO_y catalysts. The ease of synthesis and the high catalytic activity of the as-synthesized Au-loaded mesoporous Fe_2O_3 nanoflakes suggest their promising potential as catalysts for commercial CO oxidation.

Conflicts of interest
There are no conflicts to declare.

Notes and references

1. P. Sudarsanam, B. Mallesham, P. S. Reddy, D. Großmann, W. Grünert and B. M. Reddy, *Appl. Catal. B*, 2014, **144**, 900-908.
2. I. H. Kim, H. O. Seo, E. J. Park, S. W. Han and Y. D. Kim, *Sci. Rep.*, 2017, **7**, 40497.
3. S. Gatla, D. Aubert, G. Agostini, O. Mathon, S. Pascarelli, T. Lunkenbein, M. G. Willinger and H. Kaper, *ACS Catal.*, 2016, **6**, 6151-6155.
4. J. R. Gaudet, A. de la Riva, E. J. Peterson, T. Bolin and A. K. Datye, *ACS Catal.*, 2013, **3**, 846-855.
5. M. Haruta, S. Tsubota, T. Kobayashi, H. Kageyama, M. J. Genet and B. Delmon, *J. Catal.*, 1993, **144**, 175-192.
6. M. Daté and M. Haruta, *J. Catal.*, 2001, **201**, 221-224.
7. S. Tanaka, J. Lin, Y. V. Kaneti, S.-I. Yusa, Y. Jikihara, T. Nakayama, M. B. Zakaria, A. A. Alshehri, J. You, M. S. A. Hossain and Y. Yamauchi, *Nanoscale*, 2018, **10**, 4779-4785.
8. Y. Wang, H. Arandiyan, J. Scott, A. Bagheri, H. Dai and R. Amal, *J. Mater. Chem. A*, 2017, **5**, 8825-8846.
9. S. Tanaka, Y. V. Kaneti, R. Bhattacharjee, M. N. Islam, R. Nakahata, N. Abdullah, S.-I. Yusa, N.-T. Nguyen, M. J. A. Shiddiky, Y. Yamauchi and M. S. A. Hossain, *ACS Appl. Mater. Interfaces*, 2018, **10**, 1039-1049.
10. F. Jiao, J.-C. Jumas, M. Womes, A. V. Chadwick, A. Harrison and P. G. Bruce, *J. Am. Chem. Soc.*, 2006, **128**, 12905-12909.
11. X. Xu, R. Cao, S. Jeong and J. Cho, *Nano Lett.*, 2012, **12**, 4988-4991.
12. A. Mitra, C. Vázquez-Vázquez, M. A. López-Quintela, B. K. Paul and A. Bhaumik, *Microporous Mesoporous Mater.*, 2010, **131**, 373-377.
13. T. Brezesinski, M. Groenewolt, M. Antonietti and B. Smarsly, *Angew. Chem. Int. Ed.*, 2006, **45**, 781-784.
14. Y. V. Kaneti, R. R. Salunkhe, N. L. Wulan Septiani, C. Young, X. Jiang, Y.-B. He, Y.-M. Kang, Y. Sugahara and Y. Yamauchi, *J. Mater. Chem. A*, 2018, **6**, 5971-5983.
15. I. Saptiama, Y. V. Kaneti, Y. Suzuki, K. Tsuchiya, N. Fukumitsu, T. Sakae, J. Kim, Y. M. Kang, K. Ariga and Y. Yamauchi, *Small*, 2018, **14**, 1800474.
16. E. Mendelovici, R. Villalba and A. Sagarzazu, *J. Mater. Sci. Lett.*, 1990, **9**, 28-31.
17. J. R. Copeland, I. A. Santillan, S. M. Schimming, J. L. Ewbank and C. Sievers, *J. Phys. Chem. C*, 2013, **117**, 21413-21425.
18. T. V. Choudhary and D. W. Goodman, *Top. Catal.*, 2002, **21**, 25-34.
19. A. A. Alshehri and K. Narasimharao, *J. Nanomater.*, 2017, **2017**, 14.
20. T. Tabakova, V. Idakiev, D. Andreeva and I. Mitov, *Appl. Catal. A*, 2000, **202**, 91-97.
21. T. Akita, Y. Maeda and M. Kohyama, *J. Catal.*, 2015, **324**, 127-132.
22. Z. Zhong, J. Ho, J. Teo, S. Shen and A. Gedanken, *Chem. Mater.*, 2007, **19**, 4776-4782.
23. J. Guzman and B. C. Gates, *J. Am. Chem. Soc.*, 2004, **126**, 2672-2673.
24. Q. Yao, C. Wang, H. Wang, H. Yan and J. Lu, *J. Phys. Chem. C*, 2016, **120**, 9174-9183.